Journal of Medical Imaging

MedicalImaging.SPIEDigitalLibrary.org

ART 3.5D: an algorithm to label arteries and veins from three-dimensional angiography

Beatrice Barra
Elena De Momi
Giancarlo Ferrigno
Guglielmo Pero
Francesco Cardinale
Giuseppe Baselli

SPIE.

Beatrice Barra, Elena De Momi, Giancarlo Ferrigno, Guglielmo Pero, Francesco Cardinale, Giuseppe Baselli, "ART 3.5D: an algorithm to label arteries and veins from three-dimensional angiography," *J. Med. Imag.* **3**(4), 044002 (2016), doi: 10.1117/1.JMI.3.4.044002.

ART 3.5D: an algorithm to label arteries and veins from three-dimensional angiography

Beatrice Barra,[a,*] Elena De Momi,[a] Giancarlo Ferrigno,[a] Guglielmo Pero,[b,c] Francesco Cardinale,[b,c] and Giuseppe Baselli[a]
[a]Politecnico di Milano, Electronic Information and Bioengineering Department, Piazza Leonardo da Vinci, 32, Milano 20133, Italy
[b]Niguarda Hospital, "Claudio Munari" Center for Epilepsy Surgery, Piazza Ospedale Maggiore 3, Milano 20162, Italy
[c]Niguarda Hospital, Department of Neuroradiology, Piazza Ospedale Maggiore, 3, Milano 20162, Italy

Abstract. Preoperative three-dimensional (3-D) visualization of brain vasculature by digital subtraction angiography from computerized tomography (CT) in neurosurgery is gaining more and more importance, since vessels are the primary landmarks both for organs at risk and for navigation. Surgical embolization of cerebral aneurysms and arteriovenous malformations, epilepsy surgery, and stereoelectroencephalography are a few examples. Contrast-enhanced cone-beam computed tomography (CE-CBCT) represents a powerful facility, since it is capable of acquiring images in the operation room, shortly before surgery. However, standard 3-D reconstructions do not provide a direct distinction between arteries and veins, which is of utmost importance and is left to the surgeon's inference so far. Pioneering attempts by true four-dimensional (4-D) CT perfusion scans were already described, though at the expense of longer acquisition protocols, higher dosages, and sensible resolution losses. Hence, space is open to approaches attempting to recover the contrast dynamics from standard CE-CBCT, on the basis of anomalies overlooked in the standard 3-D approach. This paper aims at presenting algebraic reconstruction technique (ART) 3.5D, a method that overcomes the clinical limitations of 4-D CT, from standard 3-D CE-CBCT scans. The strategy works on the 3-D angiography, previously segmented in the standard way, and reprocesses the dynamics hidden in the raw data to recover an approximate dynamics in each segmented voxel. Next, a classification algorithm labels the angiographic voxels and artery or vein. Numerical simulations were performed on a digital phantom of a simplified 3-D vasculature with contrast transit. CE-CBCT projections were simulated and used for ART 3.5D testing. We achieved up to 90% classification accuracy in simulations, proving the feasibility of the presented approach for dynamic information recovery for arteries and veins segmentation. © *2016 Society of Photo-Optical Instrumentation Engineers (SPIE)* [DOI: 10.1117/1.JMI.3.4.044002]

Keywords: contrast-enhanced cone-beam CT; brain angiography; classification of veins and arteries.

Paper 16088R received Jun. 1, 2016; accepted for publication Nov. 1, 2016; published online Nov. 29, 2016.

1 Introduction

Segmentation and visualization of brain vessels are important in many neurological diagnostic and therapeutic applications. Despite the advent of several noninvasive angiographic techniques, indications for catheter angiography are still numerous.[1] Embolization of cerebral arteriovenous malformations (AVMs), or their radiosurgical treatment, makes the three-dimensional (3-D) reconstruction of brain vasculature of utmost importance.[2,3] In addition, several studies indicate that 3-D visualization of brain vasculature within multimodal imaging proved to be useful in epilepsy surgery, nonetheless it is still underutilized in clinical practice.[4–8] In particular, during stereoelectroencephalography (SEEG) procedures, intracerebral electrodes must be implanted avoiding vessel hurting and subsequent intracranial bleeding.[9–14] In addition to the vascular tree reconstruction, the detached visualization of arteries and veins could be advantageous to surgical treatment planning. In fact, the visualization of AVM feeding vessels, nidus, and draining veins could be easier.[15] Also, the planning of SEEG-guided radio-frequency thermal ablations[16,17] could be safer thanks to a better estimation of the risk related to arteries or veins proximity. In addition, the separate visualization of arteries and veins could be helpful when 3-D multimodal scenes are utilized to plan and perform brain resections,[5,8] providing clearer anatomical landmarks helping to compare such complex images with the surgical field.

Several techniques are used for the separation of arterial from venous structures such as magnetic resonance angiography (MRA)-based and four-dimensional (4-D) CT-based techniques.

Contrast-enhanced-MRA (CE-MRA) techniques address a phase-contrast or a time-resolved acquisition approach,[18,19] followed by correlation analysis and graph searching methods as postprocessing techniques.[20,21] In Bock et al.,[20] a correlation analysis method is employed on a 3-D MR angiogram of the lung, sampled during the breath-hold with a 3-D FLASH pulse sequence. In Sonka et al.,[22] a graph search approach is exploited consisting of a seeded region growing for vascular tree segmentation, followed by a graph search that determined the most favorable path starting from a set of points defined by the user, taking into account the morphological features in order to chose the optimal path. In Niessen et al.,[21] an enhanced artery visualization method allows one to segment large venous structures in the upper leg/abdominal region. Finally, Lei et al.[15] introduced a fuzzy connected object delineation approach and separated arteries from veins using an iterative relative fuzzy "connectedness" measure.

*Address all correspondence to: Beatrice Barra, E-mail: beatrice.barra@mail.polimi.it

2329-4302/2016/$25.00 © 2016 SPIE

In 4-D CT-based methods, several image volumes are acquired (around 20 volumes on average) while the contrast medium is flowing in the vessels, obtaining a 4-D CT perfusion (CTP) scan. This imaging method is particularly suitable for arteries and veins segmentation even if it is worse in spatial resolution with respect to standard 3-D CT scans and has a very limited temporal resolution.

In Laue et al.,[23] a method based on unsupervised classification of time intensity curves (TICs) is presented. TICs are computed as the image intensity variation over time for each voxel. A 4-D CT dataset, comprising 24 volumes, was acquired in a time window of 200 s while nonionic contrast was injected. K-means clustering was applied to TICs and three clusters were identified, namely the arteries, the veins, and the vessels outside the brain. No numerical results are reported for this work. Mendrik et al.[24] combined a CTP scan and a CT angiography (CTA). They segmented the vasculature using the Gaussian first-derivative information and separated arteries from veins using the time to peak (TTP) information. The voxels were labeled as artery or vein depending on their TTP being similar to an arterial or a venous TTP zero-crossing. Sensitivity values between 0.928 and 0.958 were obtained, together with specificity values between 0.964 and 0.985 and accuracy values between 0.961 and 0.963. Separate arteriogram and venogram were constructed. All the MRA and 4-D CT methods presented above require the acquisition of many images, with different imaging methods. Though successful, those methods are often difficult to apply in a clinical context, since the acquisition and processing of several images are expensive and time consuming for the surgeons.

This paper presents a method for arteries and veins segmentation, obtained through the postprocessing of cone-beam CT (CBCT) raw projection data together with the angiogram obtained from a CBCT digital subtraction angiography (DSA). Unlike 4-D CT techniques, the use of a standard CBCT dataset does not require any additional x-ray exposure of the patient and ensures a better resolution with respect to 4-D scans. Moreover, the CBCT represents a powerful facility, since it is capable of acquiring images in the operation room, shortly before surgery.

2 Methods

In order to label arteries and veins from CBCT scans, the algebraic reconstruction technique (ART) was extended dynamically, in order to account for dynamic changes of voxel intensity values in time, according to the progression of contrast medium. Voxel-wise dynamic variations were described by a TIC. TICs were modeled by a set of temporal basis functions in order to capture, with a minimal parameter set, regular wash-in wash-out features and approximate timing sufficient to separate arteries and veins.

2.1 *Contrast Time Profile Reconstruction*

A general linear time invariant (LTI) system is formalized as

$$\mathbf{p} = \mathbf{W}\boldsymbol{\mu}, \tag{1}$$

where $\mathbf{W}$ is the system matrix, $\boldsymbol{\mu}$ is the unknowns vector, and $\mathbf{p}$ is the measures vector. The system is

$$p_i = \sum_{j=1}^{J} w_{i,j} \cdot \mu_j = |w_{i,1}, \ldots, w_{i,J}| \cdot \begin{vmatrix} \mu_1 \\ \ldots \\ \mu_J \end{vmatrix}. \tag{2}$$

In the case of image reconstruction, p_i is a single projection element, the terms $w_{i,j}$ are the system matrix elements, and the terms μ_j are the image voxel values to be computed.

In standard CBCTs, projections are taken on the flat panel device (FPD) at discrete angles θ_k, at proportional time instants t_k:

$$\theta_k = \omega t_k \left(k = 1, \ldots, K; \omega = \frac{2\pi}{T} \right), \tag{3}$$

where T is the revolution time in the order of tens of seconds, 12 s in our protocol, and K is the number of angular samples, 360 in our protocol. Obviously, the same proportion is found between the angular increments and sampling time intervals: $\Delta\theta = \omega\Delta t$, with $\theta_k = k\Delta\theta$ and $t_k = k\Delta t$. The contrast infusion protocols are calibrated in order to provide sufficient information for a 3-D reconstruction, sufficient to angiographic segmentation. In doing this, the contrast dynamics is overlooked, with negligible artifacts relevant to the segmentation aim. Still, the overlooked information is clearly visible as shown in the projections of the common example in Fig. 1. Clearly, the information is incomplete and far from a complete 4-D dataset, since the angle of view of each time sample is bounded:

$$\theta_k = k(t_k)\Delta\theta. \tag{4}$$

Importantly, each projection angle θ_k leads to $(N \times M)_k$ projection values, p_k, where N and M are the dimensions of the FPD in pixels (Fig. 2). ART schemes work on a column vector of projections $\mathbf{p} = \text{col}|p_i|$, $(i = 1, \ldots, I, I = K \times N \times M)$. The spatial position is not evidenced, but is obviously recoverable by the vector construction rule: $i = i(\theta_k, a_m, b_n)$, where a_m and b_n are the horizontal and vertical displacements on the FPD, while θ_k is the focal spot rotation angle, which is the relevant parameter in the dynamic problem.

The presented approach extends the iterative algebraic solution from an LTI to a linear time variant (LTV) system exploiting information about system dynamics during contrast-enhanced CBCT (CE-CBCT) acquisitions. The ART was thus extended to the case of dynamic image reconstruction, accordingly named ART 3.5D.

The goal of classifying arteries and veins permits a huge reduction of the ART problem dimension by two aspects: (1) an approximate voxel-wise TIC is sufficient to evaluate the contrast TTP with the limited precision required to disentangle arteries from veins, also considering the long capillary phase; and (2) the dynamics of only the previously segmented standard angiography is considered.

Hence, the full 4-D problem of order N^4 is reduced below the order N^3 of the available CBCT projections. The following general, though heuristic, reasoning was applied, yet to be validated according to the specific dataset features: (1) the TIC is conveniently approximated by $B = 10 - 20$ basis functions, at homogenous time shifts, with $B \ll N$. In fact, given a predetermined set of basis functions, the curve is represented from the coefficients multiplying the basis functions; and (2) the arteriography projections are never fully dense, so the segmented tree is composed by order N^2 voxels, maximum. As a result, the number of

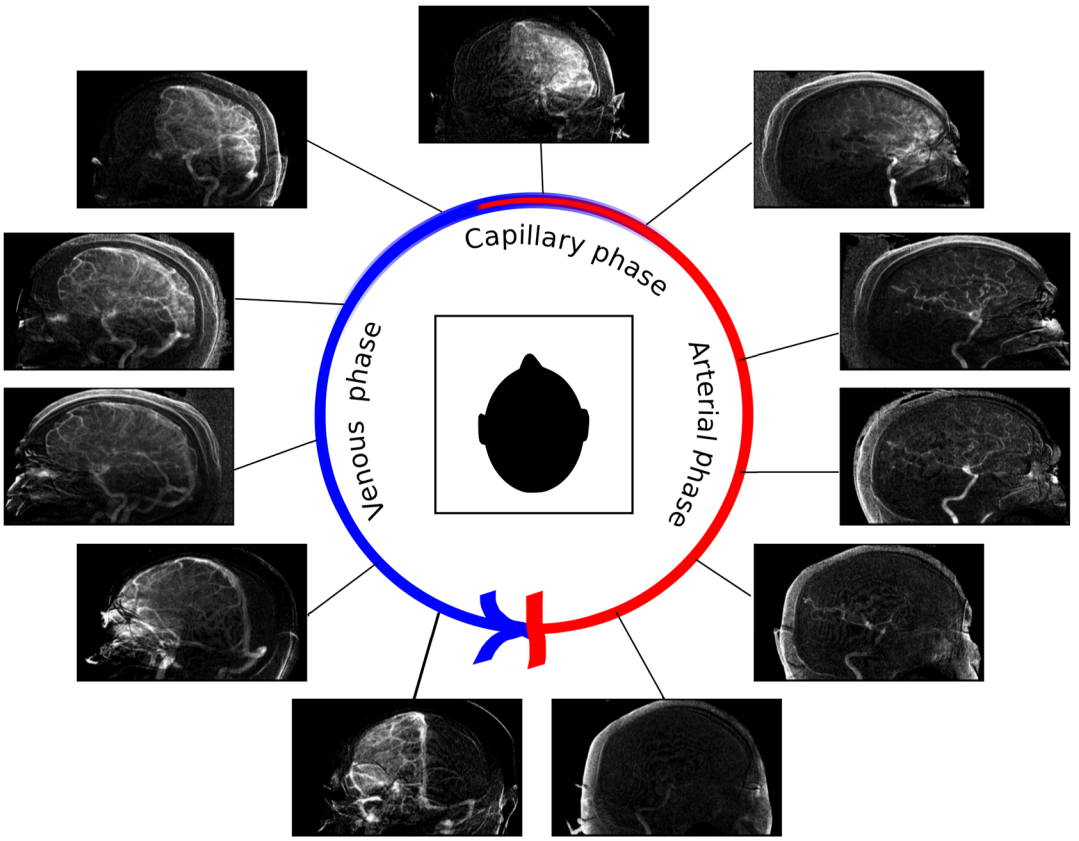

Fig. 1 Schema of the dynamic evolution of contrast flow during image acquisition. Arterial and venous phases are highlighted.

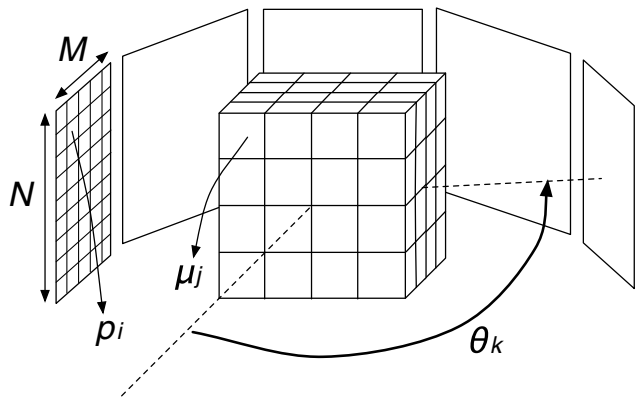

Fig. 2 Geometric schema of the acquisition process with indexed elements. p_i is a projection element, N and M are the FPD dimensions, μ_j is a voxel intensity value, and θ_k is the projection angle at time t_k.

unknowns ($\sim B \times N^2$) $\ll$ number of equations ($\sim N^3$). This reasoning was validated according to the specific dataset features. In particular, the CBCT standard acquisition protocol of the O-ARM4 (Medtronic, Minneapolis, Minnesota)[25] is taken as reference, and the acquisition parameters are listed in Table 1.

Therefore, for a Medtronic O-arm system, the number of projection results is:

$$N_p = N \times M \times N_\theta = 384 \times 1024 \times 391 \sim 153 \times 10^6, \quad (5)$$

and the number of unknowns is equal to

$$N_u = J \times B = (512 \times 512 \times 192) \times 10 \sim 503 \times 10^6, \quad (6)$$

where J is the total number of voxels in a dataset and B is the number of chosen basis functions. A reduction of a factor of 100 of the number of vascular voxel with respect to the total number of voxels in a CT image has been hypothesized and afterward

Table 1 Medtronic O-ARM4 acquisition parameters.

Image dimension in voxels (N^x_{voxel}, N^y_{voxel}, N^z_{voxel})	(512, 512, 192)
Voxel spacing (w_{voxel})	0.415 mm
Slice thickness (t_s)	0.833 mm
FPD dimension in pixel ($N \times M$)	384×1024
FPD pixel size (w_{pixel})	0.388
Rotation radius (R)	647.7 mm
Distance of FPD surface center from isocenter	520.7 mm
Number of projections (N_θ)	391
Minimum angle (θ_{min})	0 deg
Maximum angle (θ_{max})	360 deg
Acquisition time (T_a)	12 s

inspected in a real CTA dataset. Therefore, the number of unknowns reduces to

$$N_u = J \times B \times \frac{1}{100} = (512 \times 512 \times 192) \times 10 \times \frac{1}{100} \sim 5 \times 10^6, \quad (7)$$

which is lower than the number of projections. As already stated, the hypothesis on the dimension reduction was verified on a real dataset. A vessel segmentation and reconstruction were obtained through a DSA in 3-D Slicer 4.3.1.[26] The vessel reconstruction was analyzed and the voxels belonging to the vessel mask were counted resulting in an overall number of vessel voxels equal to 962,573, which is approximately 0.1% of the total number of image voxels. Then the hypothesis made is widely respected, proving the problem to be well conditioned.

With the working hypothesis proved, the TIC was modeled as a linear combination of basis functions, whose weighing coefficients had to be estimated. The basis functions set was chosen *a priori* (see Sec. 3.2) and included in the system matrix $\mathbf{W}$. A new system matrix, $\mathbf{W_d}$, was introduced that combined the static weights, $w_{i,j}$, and the samples of the basis functions at each projection time, t_k. Simple mathematical manipulations show how the system matrix was expanded and the LTI problem rephrased to an LTV one. First, the j'th voxel intensity, μ_j, was replaced by a time function for the dynamic problem, the TIC profile $= \mu_j(t)$. This time curve of each voxel was then modeled through a linear combination of basis functions, as previously introduced:

$$\mu_j(t) = \sum_{b=0}^{B} d_{j,b} \cdot q_b(t) = |\, d_{j,0} \quad \ldots \quad d_{j,B} \,| \cdot \begin{vmatrix} q_0(t) \\ \ldots \\ q_B(t) \end{vmatrix}, \quad (8)$$

where the coefficients $d_{j,b}$ weight the B basis functions. The set of weights $d_{j,b}$ corresponds to the new set of unknowns, for J angiographic voxels, where J is the number of voxels belonging to the vascular tree. Substituting the term $\mu_j(t)$ [expressed in Eq. (8)] in the LTI problem formulation [Eq. (2)], the following equation is obtained:

$$p_i = \sum_{j=1}^{J} w_{i,j} \cdot \mu_j(t) = \sum_{j=1}^{J} w_{i,j} \cdot \left[\sum_{b=1}^{B} d_{j,b} \cdot q_b(t_k) \right] \quad (9)$$

and

$$p_i = \sum_{j=1}^{J} \sum_{b=1}^{B} q_b(t_k) \cdot w_{i,j} \cdot d_{j,b}. \quad (10)$$

Since both the static system matrix elements $w_{i,j}$ and the basis function samples $q_b(t_k)$ are fixed and object independent, the elements of a complete dynamic system matrix can be defined as

$$w^d_{i,j,b} = w_{i,j} \cdot q_b(t_k), \quad (11)$$

leading to a complete, yet unsolvable algebraic problem:

$$p_i = \sum_{j=1}^{J} \sum_{b=1}^{B} w^d_{i,j,b} \cdot d_{j,b}, \quad (12)$$

$$\mathbf{p} = \mathbf{W_d} \boldsymbol{\mu}. \quad (13)$$

The new dynamic system matrix $\mathbf{W_d}$ has the same number of rows I as W, but a column number increased to $J \times B$ as the dimension of the vector of unknowns $\boldsymbol{\mu}_\mathbf{d}$. A convenient ordering of $\boldsymbol{\mu}_\mathbf{d}$ is by taking all basis function weights voxel-by-voxel; thus, $\mathbf{W_d}$ groups B columns per voxel, repeating J times the same order of basis functions. The prior segmentation, as said, permits to reduce dimension to a solvable problem by considering only the angiogram voxels $j\epsilon\{\text{Angio}\}$ if the subtraction among the contrast-enhanced and noncontrast-enhanced datasets is used as the projection dataset ($\mathbf{p_r} = \mathbf{p_{CE}} - \mathbf{p}$).

$$p_i = \sum_{j\epsilon\{\text{Angio}\}} \sum_{b=1}^{B} w^d_{i,j,b} \cdot d_{j,b}, \quad (14)$$

$$\mathbf{p_r} = \mathbf{W_r} \boldsymbol{\mu}_\mathbf{r}, \quad (15)$$

where $\mathbf{W_r}$ and $\boldsymbol{\mu}_\mathbf{r}$ are the system matrix and the unknowns vector reduced at the vascular voxels. Clearly, the reduced problem is object dependent and the reduction consists of eliminating the groups of B columns in $\mathbf{W_d}$ relevant to each voxel j external to the segmented vascular tree. Therefore, the proposed method retrieves dynamic information from a standard linear algebraic problem, which can be solved by a reconstruction algorithm. Once the vector of the unknowns is reconstructed, the TICs of the voxels could be obtained as a weighted sum of the basis functions.

2.2 *Classification of Arteries and Veins*

Voxel-wise classification was based on the arterial area under the curve (AUC_i^A), computed as the integral of the j'th voxel $\text{TIC}_j(t)$ up to the believed end of arterial phase T_A

$$\text{AUC}_j^A = \int_0^{T_A} \text{TIC}_j(t)\text{d}t, \quad (16)$$

and normalized by the AUC_i over the whole acquisition time T.

In fact, it comes from experimental evaluation that arterial TICs have an AUC in the first half of the curve much greater than that in the second half on the curve, while the venous TICs show a smaller AUC in the first half of the curve. Therefore the partial arterial AUC was next normalized by the entire AUC of the j'th voxel

$$\text{AUC}_j = \int_0^{T} \text{TIC}_j(t)\text{d}t, \quad (17)$$

and compared with an arterial threshold Th^A with $0 < Th^A < 1$, to be exceeded for arterial classification:

$$\frac{\text{AUC}_j^A}{\text{AUC}_j} \geq Th^A \rightarrow \text{Artery} \quad \text{else} \rightarrow \text{Vein}. \quad (18)$$

Clearly, both T_A and Th^A are the classification parameters to be adjusted according to the specific contrast infusion protocol, or even individually by some supervised (e.g., pointing a known artery) or unsupervised (e.g., automatic detection of a main artery) criterion. Also, fixing a further venous threshold might be useful, with $0 < Th^V < Th^A < 1$, where the veins are classified below Th^V while the values between the two

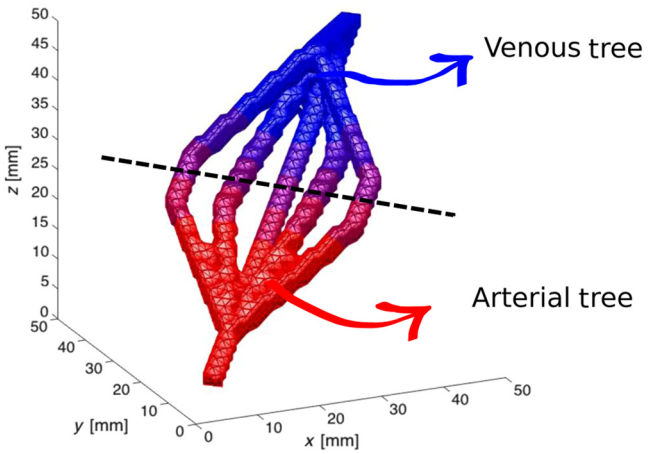

Fig. 3 Simulated vessel tree phantom. The arterial tree (lower part, in red) is separated from the venous one (upper part, in blue).

thresholds should highlight uncertain arteriography segments such as AVMs. In the present proof of concept, given the simple simulations performed, T_A was fixed at $T/2$ while the optimal value Th^A was experimentally evaluated.

3 Simulation Protocol

In order to test the behavior of the ART 3.5D algorithm, a vessel tree was simulated including the dynamic contrast flow. A set of CBCT projections was computed on it to blindly compute the TICs by ART 3.5D and next perform the artery/vein classification to be compared with the generated ground truth. The vessel tree, represented in Fig. 3, is composed of seven segments, two of them being shunted. The absence of a capillary phase, though not physiologic, made the separation of arteries and veins more critical, hence this simplified anatomy was considered as suitable to challenge the classification rule. The diameter of the vessels is 0.41 mm, the whole image dimension in voxels is $20 \times 20 \times 20$, and the dimension of the isotropic voxels is 1 mm^3. The intensity curve for each voxel j was simulated as a sigmoidal curve of intensity over time (μ_j):

$$\mu_j(t) = \frac{1}{1 + e^{-c(t-t_f)}}, \tag{19}$$

where c is the parameter slope and t_f is the inflection point in time. The sigmoid curve was selected among other shapes analyzing arteriography images. In addition, arteriography images were studied for the choice of a range of reasonable slope values for the sigmoids. The methodology used for the slope value selection is described in Sec. 3.1. For each simulation, the root mean square error (RMSE) was evaluated on the reconstructed TIC for each voxel (TIC_j), with respect to the TICs of the simulated dynamic vessel tree phantom ($\widehat{\mathrm{TIC}}_j$):

$$\mathrm{RMSE} = \frac{\sqrt{\sum_{j=1}^{n} \left(\mathrm{TIC}_j - \widehat{\mathrm{TIC}}_j\right)^2}}{n}, \tag{20}$$

where n is the number of TIC samples. In addition, contingency tables were evaluated for both arteries and veins classification, and sensitivity and specificity were computed. Moreover, the dependency of the evaluation indices on the simulated contrast transit dynamics was evaluated.

3.1 *Sigmoid Slope Selection*

We inspected an arteriography dataset acquired during the standard SEEG protocol at Ospedale Niguarda di Milano. The patient had given informed consent and the dataset was anonymized. The arteriography dataset is composed of 21 frames, acquired in 12 s after the injection of 40 cc of contrast medium in 1 s. From the arteriography, 12 arterial voxels and 12 venous voxels were manually selected (Fig. 4). For each of them, the contrast transit curve over time was considered (Fig. 5) in order to estimate the curve slope in the rising of contrast concentration, and the slope of the curve (s) was computed as the ratio among the intensity difference among two subsequent frames (ΔI) and the time elapsed among the two image samples (Δt):

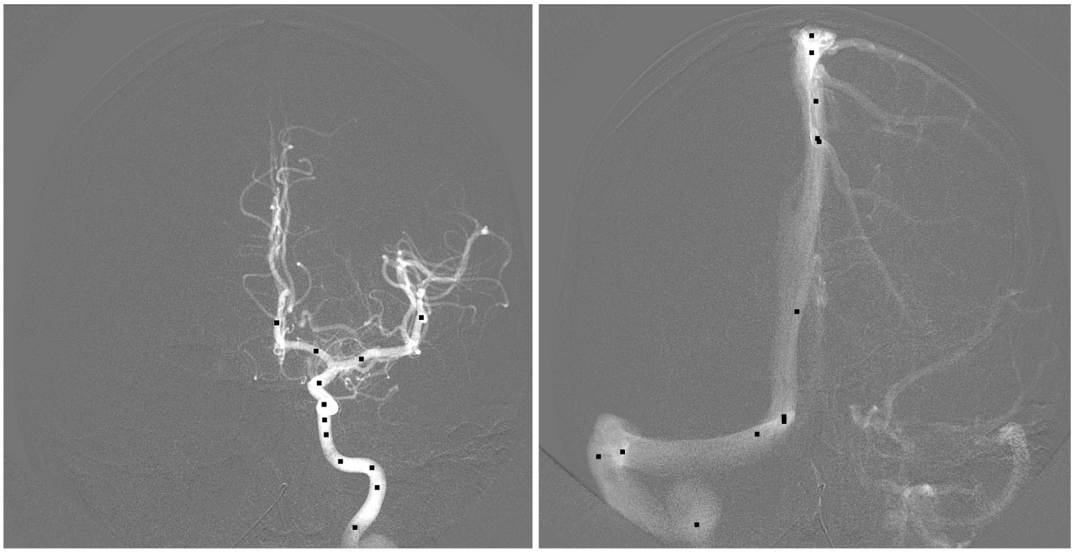

Fig. 4 Selected (a) arterial and (b) venous voxels in arteriography images are marked with black dots.

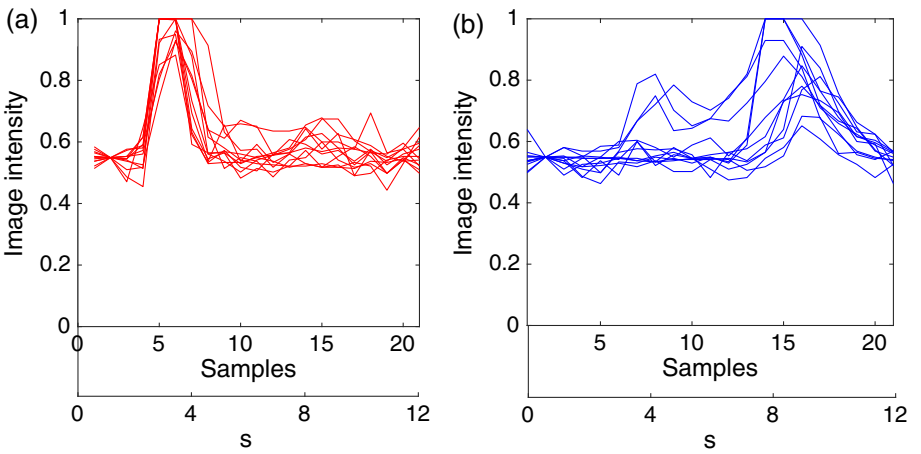

Fig. 5 TIC of (a) arterial (red) and (b) venous (blue) voxels, for voxels selected as shown in Fig. 4.

$$s = \frac{\Delta I}{\Delta t}. \tag{21}$$

Since the dynamics in the vessel phantom was modeled with sigmoidal dynamics, the slope values were interpreted as the derivative of the sigmoidal curve (μ_j) at the inflection point t_f, namely

$$s = \frac{d}{dt}\mu|_{t_f} = \frac{c}{4}. \tag{22}$$

Therefore, the varying parameter c was computed as $c = 4\ s$. Sigmoidal curves with values of c corresponding to the median, 25th and 75th quartiles, of arterial slope values were applied on the arterial voxels of the vessel tree phantom, and in the same way, in the venous voxels of the vessel tree phantom, sigmoidal curves with values of c corresponding to the median, 25th and 75th quartiles, of venous slope values were set. Table 2 summarizes all conditions for the experimental simulations.

3.2 *Basis Functions Selection*

Several basis functions sets have been taken into account including step-shaped, triangular, and logistic basis functions. The step-shaped basis functions proved to be the most suitable, due to their relative squareness. The number of basis functions needed to model a time profile along 12 s, which is the acquisition time, was evaluated between 10 and 20. Moreover, the possibility of fitting real arterial and venous TICs with such basis functions has been evaluated on the arteriography data, leading to the conclusion that the reduction in accuracy was small enough (RMSE is 0.012) to justify and rationalize the great benefit gained in reducing the dimensionality of the problem.

Table 2 Arterial and venous slope values imposed in different setups.

Setups	Arterial slope	Venous slope
Setup 1	25th q = 0.2265	25th q = 0.1167
Setup 2	Median = 0.3006	Median = 0.1331
Setup 3	75th q = 0.3157	75th q = 0.2114

4 Experimental Protocol

The ART 3.5 algorithm was also applied to a clinical dataset in order to verify the correct functioning on a real CTA. The dataset was acquired at Ospedale Niguarda di Milano, following the CBCT standard acquisition protocol of the O-ARM4. The patient had given informed consent and the dataset was anonymized. Since the dimensionalities of a real CTA dataset introduce a very high-computational time and large memory occupation, the resolution of the dataset was reduced to a factor of 6. The number of voxels has been reduced from $192 \times 512 \times 512$ to $32 \times 85 \times 85$, while the dimensions of a voxel, originally $0.415 \times 0.415 \times 0.833$ mm^3, became $2.5 \times 2.5 \times 5$ mm^3. The obtained level of resolution limits the reconstruction to the largest arteries and veins, allowing a proof of concept on real clinical data, without introducing a far too high-computational complexity. In order to evaluate the outcome of the ART 3.5D algorithm, arteriography images have been used as reference and ground truth. In fact, in such bidimensional images, the temporal evolution of the contrast medium in vessels from one frame to another is clearly distinguishable, allowing the identification of frames belonging to arterial and venous phases. For both the arterial and venous frames, a projection along the sagittal axis comprising all the arterial frames and another one comprising all venous frames have been produced, obtaining a arterial and venous bidimensional segmentation of arterial and venous pixels on the frontal plane. The arterial and venous reconstructions from the ART 3.5D underwent the same process, meaning that a maximum intensity projection has been performed on the arterial and venous volumes along the sagittal plane. Subsequently, arteriography-based projections and reconstruction-based projections have been qualitatively compared, for a proof of concept. No statistics on arteries and veins classification performance has been performed due to the lack of other clinical datasets, which would have guaranteed a sufficient number for statistical evaluation.

5 Results

The results obtained performing simulation with the selected slope values are shown below. The RMSE results are shown in Table 3. The RMSE slightly increased with increasing slope values, though displaying low values in all simulation setups. Moreover, the trend of RMSE error over the algorithm iterations was inspected for gaining insight on the algorithm convergence. In this simple simulation context, the first two

Table 3 RMSE among reconstructed and simulated profiles in the three experimental setups.

Setups	RMSE
Setup 1	9.2177×10^{-4}
Setup 2	9.3728×10^{-4}
Setup 3	9.7461×10^{-4}

iterations are actually the most important ones in the process, resulting in the 95% of the reduction in RMSE error.

The contingency tables for the arteries classification are shown in Table 4. The correct classification of arteries slightly increases with increasing slope values. The contingency tables for veins classification are shown in Table 5. The correct classification of veins was slightly better in simulation setups 1 and 2, and the veins true negative slightly increases with increasing slope values.

The sensitivity, specificity, and accuracy values for arteries and veins classification in all the simulation setups are reported in Tables 6–8, respectively.

Table 4 True positive, false positive, true negative, and false negative values for arteries classification are shown for each simulation setup.

Arteries classification		Simulated	
Setup 1	(%)	P	N
	P	97.78	0.20
	N	2.22	99.80
Setup 2	P	98.85	0.19
	N	1.15	99.81
Setup 3	P	99.99	0.23
	N	0.01	99.77

Table 5 True positive, false positive, true negative, and false negative values for veins classification are shown for each simulation setup.

Veins classification		Simulated	
Setup 1	(%)	P	N
	P	92.63	0.03
	N	7.37	99.97
Setup 2	P	93.18	0.01
	N	6.82	99.99
Setup 3	P	92.27	0.01
	N	7.73	99.99

Table 6 Sensitivity values for arteries and veins classification for each simulation setup reported as a percentage of all the classified voxels.

Sensitivity (%)	Arteries	Veins
Setup 1	99.79	99.97
Setup 2	99.81	99.99
Setup 3	99.77	1

Table 7 Specificity values for arteries and veins classification for each simulation setup reported as a percentage of all the classified voxels.

Specificity (%)	Arteries	Veins
Setup 1	97.82	93.13
Setup 2	98.86	93.62
Setup 3	1	92.83

Table 8 Accuracy values for arteries and veins classification for each simulation setup reported as a percentage of all the classified voxels.

Accuracy (%)	Arteries	Veins
Setup 1	98.79	96.30
Setup 2	99.33	96.58
Setup 3	99.89	96.14

Additionally, the arteriography-based and reconstruction-based arterial and venous segmentations on the frontal plane are shown, respectively, in Figs. 6 and 7. The arterial and venous trees' shapes obtained with the ART 3.5D reconstruction and segmentation are similar to the ones obtained from the arteriography data, though with strong limitations in resolution, introduced to make the computation feasible. Therefore, we consider this result as a proof of concept for the functioning of ART 3.5D on real CTA data, aware that several optimizations are needed to make it suitable for precise and reliable arteries and veins segmentation.

6 Discussion and Future Work

In this paper, a classification technique of arteries and veins is presented, which exploits CE-CBCT data with no need for extra scans, instrumentation, or contrast delivery. The ART 3.5D procedure is a postprocessing of the standard angiography, which further exploits the projection data taking into account the contrast dynamics, which had been overlooked in the standard arteriography computation. The algebraic problem solved by ART 3.5D appears to be well posed as to the proportion of projection data and the unknowns of voxel-wise description of contrast dynamics, thanks to TICs simplified by a basis function model and the reduction to the sole voxels included in the

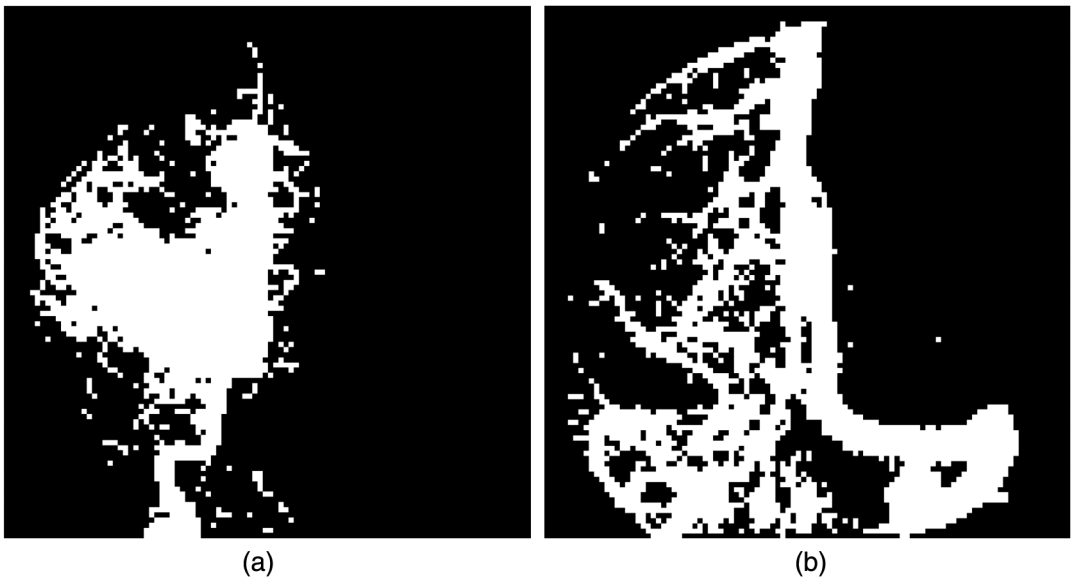

Fig. 6 (a) Arterial and (b) venous trees obtained from arteriography-based projection along the sagittal axis.

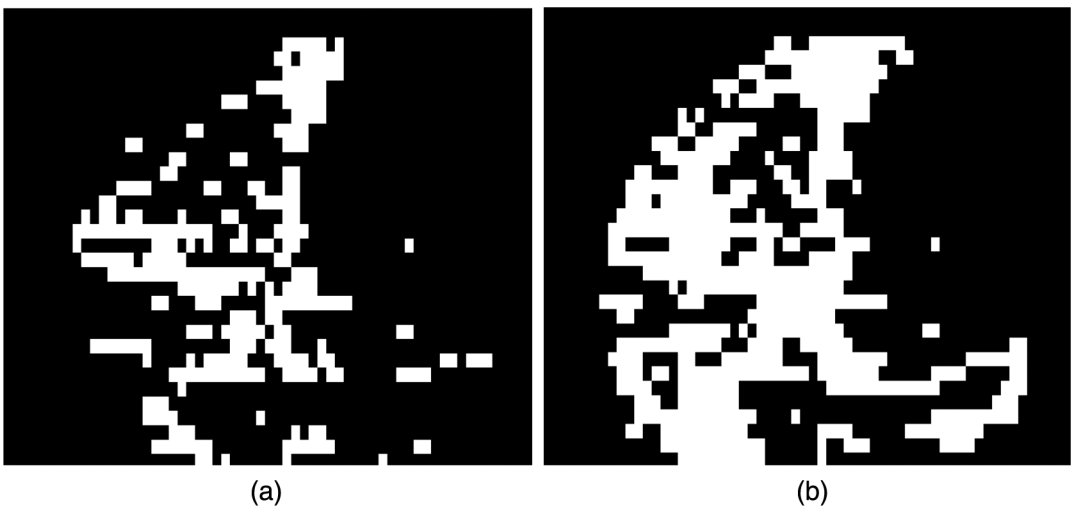

Fig. 7 (a) Arterial and (b) venous trees obtained from reconstruction-based projection along the sagittal axis.

prior angiographic segmentation. Voxel's TICs were reconstructed exploiting the implicit and usually overlooked dynamic information contained in the CBCT acquired data due to the transit of the contrast bolus. Though limited to theoretical analyses and digital simulations, the present work was able to demonstrate the feasibility of the proposed principles. An iterative algebraic technique, namely the ART 3.5D algorithm, was exploited for the TICs reconstruction. Once the TICs were reconstructed, the voxels were classified as artery or vein depending on the distribution of the AUC in time.

The reconstructed TICs presented low RMSE values, with a regularity sufficient for the next classification. The classification was evaluated computing the percentage of correctly classified voxels and incorrectly classified voxels, obtained from the comparison among the computed classification and the simulation *a priori* information. The classification showed good results, up to more than 90% of correctly classified arteries and veins. This outcome, yet limited to highly simplified angiographic simulations, is promising as to feasibility and deserves some discussion in the perspective of real data analyses. In addition, the processing of a real CTA dataset lowered in resolution was introduced, leading to a qualitative proof of concept of the suitability of the ART 3.5D algorithm for clinical data. In the latter, including hundreds of vascular branches, a higher classification error has to be expected. Nonetheless, in future developments, several improvements can be exploited, which were not introduced so far:

- Time regularization: it was limited here to a coarse separation of TICs into time-shifted basis functions, but no constraint relevant to wash-in sequence was imposed and also no insertion or temporal smoothing within the iteration cycles was attempted.
- Spatial continuity: classification after the reconstruction of TICs was performed on a voxel-wise basis. However,

region growing techniques could easily get rid of isolated misclassified voxels on the hypothesis of the continuity of vessels.

A further element in favor of reliable classifications on real datasets is represented by the wide temporal gap shown by the capillary phase of contrast transit, which is a facilitating feature not included in the present simulations. The contrast medium is rapidly washed in through the arteries, next it fades expanding in the huge network of unresolved capillaries, and next reappears in veins for the final rapid wash-out. This is easily seen by observing the sequence of projections through time and not yet exploited in our algorithm. In conclusion, the ART 3.5D algorithm introduces the possibility to account for dynamics from CE-CBCT acquisition, without requiring additional x-ray exposure to the patient or any lowering in spatial resolution. This allows for arteries and veins classification and labeling within the vascular tree, which is important in many clinical applications involving vascular disease or malformations or intervention planning.

Further analysis should also be devoted to more sophisticated classifications drawn from the TICs, beyond a sharp separation of arteries and veins. Indeed, the availability of the whole time course of contrast wash-in wash-out is foreseen as a potential tool to also classify anomalous compartments as AVMs and also provide functional indices relevant to possible insufficiencies of both the arterial and venous compartments. Further work would be needed in order to make the algorithm suitable for real images processing. In fact, currently, the computational cost of the algorithm makes unsuitable the processing of high-resolution clinical datasets. In particular, computational time limits might be brightly solved adopting an appropriate computational framework, relying on a more powerful hardware and exploiting parallel computation techniques. So far, however, it was noticed that the number of needed ART iterations was limited to two iterations. The thought that this might be due to the simple simulation context, also suggests that ART is likely to converge quickly to a solution within this type of problem framework.

Also, the ART problem dimension is lower than that of a standard 3-D static reconstruction, which is normally afforded by suitable software engineering running on standard imaging workstations. In further algorithm refinements, a major, though affordable, problem is foreseen in creating and loading the object-dependent dynamic system matrix, reduced upon the specific angiogram to be classified.

Acknowledgments

The present work has been supported and advised by Medtronic, Minneapolis, USA. Dr. Cardinale reports receiving consulting fees from Renishaw-Mayfield, since 2010.

References

1. J. C. Wojak et al., "Quality improvement guidelines for adult diagnostic cervicocerebral angiography: update cooperative study between the Society of Interventional Radiology (SIR), American Society of Neuroradiology (ASNR), and Society of Neurointerventional Surgery (SNIS)," *J. Vasc. Interventional Radiol.* **26**(11), 1596–1608 (2015).
2. D. Babin et al., "Brain blood vessel segmentation using line-shaped profiles," *Phys. Med. Biol.* **58**(22), 8041–8061 (2013).
3. M. G. Safain et al., "Use of cone-beam computed tomography angiography in planning for gamma knife radiosurgery for arteriovenous malformations: a case series and early report," *Neurosurgery* **74**(6), 682–696 (2014).
4. M. Nowell et al., "Utility of 3D multimodality imaging in the implantation of intracranial electrodes in epilepsy," *Epilepsia* **56**(3), 403–413 (2015).
5. F. Cardinale et al., "Stereoelectroencephalography: surgical methodology, safety, and stereotactic application accuracy in 500 procedures," *Neurosurgery* **72**(3), 353–366 (2013).
6. F. Cardinale, "Talairach methodology in the era of 3D multimodal imaging: the song remains the same, but catchier, and therefore more helpful for clinical decision making and surgical planning in epilepsy surgery," *Epilepsia* **56**(6), 976–977 (2015).
7. F. Cardinale et al., "Cerebral angiography for multimodal surgical planning in epilepsy surgery: description of a new three-dimensional technique and literature review," *World Neurosurg.* **84**(2), 358–367 (2015).
8. F. Cardinale et al., "Talairach methodology in the multimodal imaging and robotics era," in *Stereotaxy and Epilepsy Surgery*, J. M Scarabin, Ed., pp. 245–272, John Libbey Eurotext, Montrouge (2012).
9. M. A. Zuluaga et al., "SEEG trajectory planning: combining stability, structure and scale in vessel extraction," *Lect. Notes Comput. Sci.* **8674**, 651–658 (2014).
10. F. Cardinale, "Stereotactic robotic application accuracy is very high in 'in-vivo' procedures," *Stereotactic Funct. Neurosurg.* **93**(1), 68–68 (2015).
11. E. De Momi et al., "Automatic trajectory planner for stereoelectroencephalography procedures: a retrospective study," *IEEE Trans. Biomed. Eng.* **60**(4), 986–993 (2013).
12. E. De Momi et al., "Multi-trajectories automatic planner for stereoelectroencephalography (SEEG)," *Int. J. Comput. Assisted Radiol. Surg.* **9**(6), 1087–1097 (2014).
13. J. P. Mullin et al., "Is SEEG safe? A systematic review and meta-analysis of stereo-electroencephalography–related complications," *Epilepsia* **57**(3), 386–401 (2016).
14. J. González-Martnez et al., "Technique, results, and complications related to robot-assisted stereoelectroencephalography," *Neurosurgery* **78**(2), 169–180 (2016).
15. T. Lei et al., "Artery-vein separation via MRA-an image processing approach," *IEEE Trans. Med. Imaging* **20**(8), 689–703 (2001).
16. M. Cossu et al., "Stereoelectroencephalography-guided radiofrequency thermocoagulation in the epileptogenic zone: a retrospective study on 89 cases," *J. Neurosurg.* **123**(6), 1358–1367 (2015).
17. M. Guénot et al., "SEEG-guided RF thermocoagulation of epileptic foci: feasibility, safety, and preliminary results," *Epilepsia* **45**(11), 1368–1374 (2004).
18. D. Bluemke et al., "3D contrast enhanced phase contrast angiography: utility for arterial/venous segmentation," in *ISMRM Proc.*, Vol. **2**, p. 1237 (1999).
19. T. Foo et al., "A novel method for MR arterial and venous discrimination using gated phase contrast and VENC selection," in *ISMRM Proc.*, Vol. **3**, p. 2182 (1999).
20. M. Bock et al., "Artery-vein separation in 3D contrast enhanced pulmonary MRA using correlation," in *ISMRM Proc.*, Vol. **1**, p. 486 (1999).
21. W. Niessen et al., "Enhanced artery visualization in blood pool MRA: results in the peripheral vasculature," *Lect. Notes Comput. Sci.* **1613**, 340–345 (1999).
22. M. Sonka, R. Stefancik, and S. Tadikonda, "Feasibility of automated separation of arteries and veins using a graph searching," in *ISMRM Proc.*, Vol. **3**, p. 2183 (1999).
23. H. Laue et al., "Automated artery and vein detection in 4D-CT data with an unsupervised classification algorithm of the time intensity curves," *Proc. SPIE* **8669**, 86691W (2013).
24. A. Mendrik et al., "Automatic segmentation of intracranial arteries and veins in four-dimensional cerebral CT perfusion scans," *Med. Phys.* **37**(6), 2956–2966 (2010).
25. Medtronic, https://www.medtronic.com (29 September 2016).
26. Slicer, https://www.slicer.org (29 September 2016).

Beatrice Barra received her MSc degree in biomedical engineering from Politecnico di Milano in 2015. Sponsored by a scholarship from the Swiss National Centre of Competence in Research (NCCR) Robotics, she worked as a research fellow at the Ecole Polytechnique Federale de Lausanne. Now she is a PhD candidate at the University of Fribourg, Switzerland, working on cervical epidural electrical stimulation for spinal cord injury recovery. Her research interests include bioimaging, surgical robotics, and neuroprostheses.

Elena De Momi received her MSc degree in biomedical engineering in 2002 and her PhD in bioengineering in 2006. She is currently an assistant professor in the Electronic Information and Bioengineering Department (DEIB) of Politecnico di Milano. Her academic interests include image processing, virtual environments, augmented reality and simulators, teleoperation, haptics, medical robotics, and neuromechanics. She participated in several EU funded projects in the field of surgical robotics (ROBOCAST, ACTIVE, and EuRoSurge). She is currently a PI for POLIMI of the EDEN2020 project.

Giancarlo Ferrigno received his MSc degree in electronic engineering in 1983 and his PhD in bioengineering in 1990. In 2008, he founded the Neuroengineering and Medical Robotics Laboratory. He has taught several courses in the field of artificial intelligence, biosensors, robotics, and basic biomedical engineering. In the last years, he has been the European Coordinator of three FP7 EU projects in the ICT topic: ROBOCAST (2008–2010), ACTIVE (2011–2015), and MUNDUS (2010–2013). Current personal active funding is ASI 2013-065-R.0-BICE.

Guglielmo Pero is a neurointerventionalist in the Department of Neuroradiology of the Niguarda Ca' Granda Hospital, Milan, Italy. His activity is focused on the endovascular treatment of cerebral vascular diseases, mainly acute ischemic stroke, cerebral aneurysms, cerebral arteriovenous malformations, and dural arteriovenous fistulas. His activity also includes diagnostic neuroradiology with experience in advanced techniques with both magnetic resonance and computed tomography.

Francesco Cardinale serves as a neurosurgeon in the "Claudio Munari" Center for Epilepsy Surgery, Niguarda Hospital, Milano, Italy. His activity focuses on stereotactic methodology for implanting intracerebral electrodes aimed to perform SEEG monitoring and on brain resective surgery. His research focuses mainly on advanced neuroimaging processing for surgical planning and on robotic-aided surgery.

Giuseppe Baselli received his MSc degree in electrical engineering, bioengineering track, from the Politecnico di Milano, cum laude, in 1983. Since 2001, he has been a full professor in bioengineering at the same university. He teaches a course on bioengineering for physiological control systems and one on methods for biomedical images. He is the author of about 120 journal papers. His research interests are mainly in cardiovascular regulation modeling and in the reconstruction and analysis of biomedical images.